





Article

Mapping Recent Lava Flows at Mount Etna Using Multispectral Sentinel-2 Images and Machine Learning Techniques

Claudia Corradino ^{1,*} , Gaetana Ganci ¹ , Annalisa Cappello ¹ , Giuseppe Bilotta ¹, Alexis Hérault ^{1,2} and Ciro Del Negro ¹ 

¹ Istituto Nazionale di Geofisica e Vulcanologia, Sezione di Catania, Osservatorio Etneo, 95125 Catania, Italy

² Conservatoire National des Arts et Métiers, Laboratoire Modélisation Mathématique et Numérique, 75003 Paris, France

* Correspondence: claudia.corradino@ingv.it

Received: 22 July 2019; Accepted: 14 August 2019; Published: 16 August 2019



Abstract: Accurate mapping of recent lava flows can provide significant insight into the development of flow fields that may aid in predicting future flow behavior. The task is challenging, due to both intrinsic properties of the phenomenon (e.g., lava flow resurfacing processes) and technical issues (e.g., the difficulty to survey a spatially extended lava flow with either aerial or ground instruments while avoiding hazardous locations). The huge amount of moderate to high resolution multispectral satellite data currently provides new opportunities for monitoring of extreme thermal events, such as eruptive phenomena. While retrieving boundaries of an active lava flow is relatively straightforward, problems arise when discriminating a recently cooled lava flow from older lava flow fields. Here, we present a new supervised classifier based on machine learning techniques to discriminate recent lava imaged in the MultiSpectral Imager (MSI) onboard Sentinel-2 satellite. Automated classification evaluates each pixel in a scene and then groups the pixels with similar values (e.g., digital number, reflectance, radiance) into a specified number of classes. Bands at the spatial resolution of 10 m (bands 2, 3, 4, 8) are used as input to the classifier. The training phase is performed on a small number of pixels manually labeled as covered by fresh lava, while the testing characterizes the entire lava flow field. Compared with ground-based measurements and actual lava flows of Mount Etna emplaced in 2017 and 2018, our automatic procedure provides excellent results in terms of accuracy, precision, and sensitivity.

Keywords: volcano hazard monitoring; satellite remote sensing; artificial networks; automatic detection; Sentinel Mission; Pléiades Mission

1. Introduction

1.1. Mapping Lava Flows

Lava flow-forming eruptions are a frequent hazard that impacts populations and properties at a number of volcanoes worldwide [1–4]. Mapping of active lava flows is therefore a valuable source of information to document the ongoing eruptions [5], while yielding insights into how lava flow fields develop that are necessary for predicting future flow behavior [6–10]. Although lava fields are mapped usually through ground-based surveys [11,12] or more recently with Unmanned Aerial Vehicles (UAV) in the air [13,14], satellite remote sensing offers an overall view of active lava flows, while avoiding the difficulties of working in hazardous locations [15,16].

The areal extent of active lava flows is challenging to record with traditional field methods because of the large size of flow fields and the often-limited accessibility of volcanic areas. Moreover, analyzing

small portions of a lava flow field may give unrepresentative results of the entire lava flow during the course of the eruption [17]. Thus, remote sensing techniques are considered a safer and more robust alternative approach capable of providing a more comprehensive survey of the whole lava flow field, which is essential when attempting to monitor lava flow hazards during volcanic eruptions [18,19]. The multispectral nature of the data and the repeated coverage of extensive volcanic terrains are major advantages of satellite remote sensing techniques [20].

An ever-increasing number of space borne sensors continue to provide a wealth of high-quality multispectral data. Optical images from satellites have been widely exploited to map lava flows and their associated spectral properties [21–23]. Satellite data in the visible, infrared, and thermal portions of the electromagnetic spectrum contain reflectance and emittance information about lava surfaces of different age and nature [18,24,25], and therefore can be used to discriminate fresh lava flows in terms of mineralogical, textural and compositional differences [26,27]. However, in optical images, it can be difficult to distinguish between weathered lava surfaces and assess their relative age due to the similarity in their chemical and surface characteristics. Furthermore, using optical satellite imagery requires that affected area be clouds-free and this often does not apply.

Radar satellite data provide a solution to this visibility disadvantage by enabling the detection of morphological changes associated with volcanic activity at any time, including nighttime or when the area of interest is covered by clouds [28,29]. However, the mapping of extensive lava flows from satellite radar data requires specific acquisition strategies. A widely-adopted strategy is based on the coherence analysis of Synthetic Aperture Radar (SAR) images, where two images recorded at two different times are compared and the lava flows are identified from low coherence areas [30–32]. An alternative strategy is based on the combination of SAR images with visible, infrared, and thermal satellite data [33,34]. However, using SAR images presents some disadvantages, such as the ambiguity of what de-correlated regions represent, persistent decorrelation masking new activity, and problems with mapping flows that enter vegetation [31].

Another remote-sensing technique that can be used to extract recent lava flow fields is differencing of pre-eruptive and post-eruptive digital elevation models (DEMs) produced using high-resolution stereo optical imagery [15,35,36]. Unfortunately, pre-eruption high-resolution topography is rarely available at poorly monitored volcanoes, and lava flow fields can only be detected if their thickness is higher than the minimum uncertainty associated with the DEMs [22]; therefore, this technique is generally not suitable during effusive crises.

The role of the pre- and post-eruptive images has been shown to be crucial in the previous well-established techniques since the differential information between them is highly related to the newly emplaced lava flow. Pre- and post-eruptive optical remote images could be used to manually trace new lava flows, but differences in the acquisition times lead to differences in the environmental condition of the imaged area, thus making this task hard to automate.

Nowadays, machine learning techniques have been widely exploited in image processing tasks [37–40]. Among them, artificial neural network models (ANNs) have been shown to be well-suited for complex data classification [41–43]. ANNs have demonstrated excellent performance in different tasks [44–46], such as pattern recognition, in a wide variety of scientific and industrial applications [47–50]. In the design of an ANN classifier, training data have to be representative of the phenomena under investigation. However, big amount of data are not always available, thus other strategies to limit the size of the training dataset may be necessary [51]. Cascading different techniques represents a valuable solution to enhance the learning performance [52,53].

Here, we present a novel classifier based on machine learning techniques designed to classify pixels related to recent lava flows from pre- and post-eruptive multispectral images combined with pre-eruptive digital topography. We utilized the Multispectral Imager (MSI) onboard Sentinel-2 satellite and the high-resolution topographic data derived from tri-stereo Pléiades-1 satellite imagery. A k-medoids unsupervised clustering is used as a strategy to minimize the ANN training dataset size. The proposed ANN is trained by using the “Bayesian regularization” training function [54], thus the

ANN will be referred to as BNN (i.e., Bayesian Neural Network). In particular, a small number of points belonging to the cooled lava flow are used to feed the BNN and obtain a 2D map. This approach is semi-automatic and was applied as a support instrument to map active lava flows of several recent effusive eruptions at Mount Etna.

1.2. Recent Lava Flow-Forming Eruptions at Etna Volcano

Mt Etna is one of the most active volcanoes in the world, showing a quasi-continuous activity at the summit craters and frequent events along fissures on its flanks [55,56]. Both summit and flank eruptions are likely to produce lava flows, and these present a major hazard to communities living and working in close proximity to the volcano [1]. Among the several lava flows produced by Mt Etna since the year 2000, the most damaging ones occurred in 2001 and 2002–2003. Lava flows extensively devastated tourist facilities, which are located at high altitudes on the southern and northern flanks of the volcano, with serious damage to the local economy [57]. The following flank eruptions occurred in 2004, 2006 and 2008–2009 from fissures opened at the eastern base of the Southeast Crater, one of the summit craters of Etna volcano. Fortunately, all these lava flow fields developed in the uninhabited Valle del Bove, a wide depression cutting the eastern flank of Mount Etna. It is worth to note that the 2008–2009 eruption was the longest flank eruption after the large 1991–1993 event and the second longest since the seventeenth century [58].

After the 2008–2009 flank eruption [59], the volcanic activity of Etna has shown a more explosive behavior, with an increasing number of paroxysmal events at the summit craters [55,60]. Indeed, 57 eruptive episodes occurred from 2011 to 2018, most of them characterized by the emission of lava fountains, pyroclastic material, and short-lasting lava flows [61]. A 2013 analysis of lava flow hazards and their distribution around the Etna volcano showed them to be far more dangerous than previously expected [62]. Here, we investigate the three most recent eruptive episodes occurring at Etna in February–April 2017, August 2018 and December 2018, which were characterized by lava emission forming extensive lava flow fields (Figure 1).

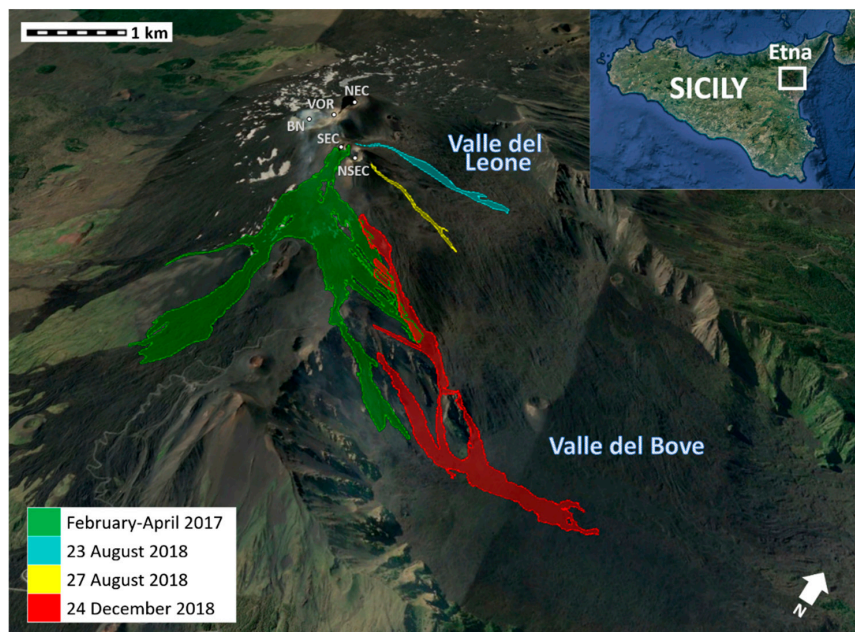


Figure 1. Google Earth 3D view (from the South-East) of Etna’s lava flows extracted from PlanetScope images used to test our classifier: February–April 2017 (green), 23 and 27 August 2018 (turquoise and yellow, respectively), and 24 December 2018 (red). “Valle del Leone” is the northeastern part of “Valle del Bove”, a large horseshoe-shaped depression located on the eastern side of the volcano. The active summit craters are also indicated: North-East Crater (NEC), Voragine (VOR), Bocca Nuova (BN), South-East Crater (SEC), and New South-East Crater (NSEC).

2. Materials and Methods

Multispectral images are a record of reflected or emitted electromagnetic energy. Each material absorbs and reflects the incoming radiation in a characteristic way [46]. Spectral reflectance of lava flows plays an important role in visible (VIS) and near-infrared (NIR) remote sensing [63–69]. However, there are three main reasons that make it difficult to map an individual lava flow from multispectral satellite data: Vegetation cover, spatial overlapping, and spectral similarity [70–72]. In particular, in high eruption frequency areas, lava flows often overlap each other; when the overlapping lava flows are erupted within a short period and have similar mineralogical composition and morphology, distinction will be made even more difficult by their similar spectral signatures [72]. Therefore, at the end of an eruption, it is often hard to identify the new emplaced lava flow over the older ones. To overcome this problem, we designed a semi-automatic supervised classifier based on machine learning techniques that simulates the human processes guiding the expert decision [73–75]. Thus, multispectral satellite data about the observed region before and after the eruption are used as input together with the pre-eruptive digital topography of the imaged area. Automated classification evaluates each pixel in a scene and then groups the pixels with similar values (e.g., digital number, reflectance, radiance) into a specified number of classes. Combining high spatial resolution digital topography with multispectral satellite data would be optimal, as it would allow a more complete extraction of the lava flow fields removing known noise without eliminating known lava flows.

2.1. Data

The MultiSpectral Imager (MSI) onboard of Sentinel-2 acquires data in 13 spectral bands, from 442.7 nm to 2202.4 nm, at 3 different spatial resolutions: 10 m (bands 2, 3, 4, 8), 20 m (bands 5, 6, 7, 8a, 11, 12) and 60 m (bands 1, 9, 10). It is a push-broom sensor with 290 km swath and a revisit time of 5 days. For lava flow mapping, we used the spectral bands at the higher spatial resolution, namely 492.4 nm (Band 2—Blue), 559.8 nm (Band 3—Green), 664.6 nm (Band 4—Red) and 832.8 nm (Band 8—NIR). We downloaded SENTINEL-2 MSI level 1 free-access data from <https://scihub.copernicus.eu/>.

Since our goal is to discriminate the most recent lava flow fields from older ones, information on the imaged area before and after the eruption has to be considered. Sentinel-2 MSI data is available twice a day, but images may be inadequate to the task due to cloud or snow covering, or other forms of corruption. Additionally, the post-eruptive images should be taken as close as possible to the end of the eruption, a constraint that may be relaxed for the pre-eruptive data. Indeed, for the post-eruptive data, rather than a single perfectly clear image taken much later, it may be better to use multiple images with partial covering or corruption, but taken closer to the end of the eruption, so that defective pixels in one image may be compensated by clear pixels in the other. Ultimately, in the best situation, the candidate post- and pre-eruptive images are recorded just a few days after and a few days before the eruption date; however, in the worst case they may have been recorded even months apart.

By only using multispectral images, misclassification errors may occur more frequently, i.e., some pixels classified as covered by fresh lava flows actually do not belong to the active flows. One significant source of error is due to the steep slopes of the volcano. Using the DEM to mask out parts of the image where the slope is very large allows us to significantly mitigate this problem. For all case studies, we utilize the 2-m resolution DEM of Etna in shaded relief form considering the solar angle at the Sentinel 2 acquisition time in order to take into account terrain shadows, thus allowing to discriminate them with respect to recent lavas. DEM was generated by very high-resolution tri-stereo optical imagery acquired by the Pléiades-1 satellite constellation on 18 July 2016 [76].

Finally, for each effusive eruption, we considered two post-eruptive Sentinel-2 images, one pre-eruptive Sentinel-2 image, and the DEM updated to 2016 to build-up the input matrix for the machine learning algorithm. In particular, each pixel of the imaged area (having a size of $N \times M$) is considered as made of 13 components, i.e., 4 values (2, 3, 4, 8 bands) for each of the two post-eruptive images and a pre-eruptive image, plus the DEM information. Thus, the input matrix for the algorithm has size $(N \times M) \times 13$.

2.2. Workflow

Once the $(N \times M) \times 13$ input matrix has been built, the first step is to pre-process the input data by filtering the areas of the images from clouds or plumes. Thus, a binary mask is created in order to remove those pixels and then applied to the input matrix.

To identify pixels belonging to the lava flow and pixels that do not, a classification method is used by exploiting the thermal information of the input data. Pixels with similar trends are grouped, creating representative clusters of the entire imaged area. In fact, the similarity of the pixels inside the same cluster reveals similar changes in time from pre- to post-eruptive images. Figure 2 shows an example of the different spectral reflectance trends of pixels belonging to two classes after the clustering stage. In particular, the 12 spectral components (4 pre- and 8 post reflectance) of the pixels belonging to a lava flow class (foreground-FG) and pixels belonging to a vegetation area (background-BG) are shown—upper and bottom, respectively.

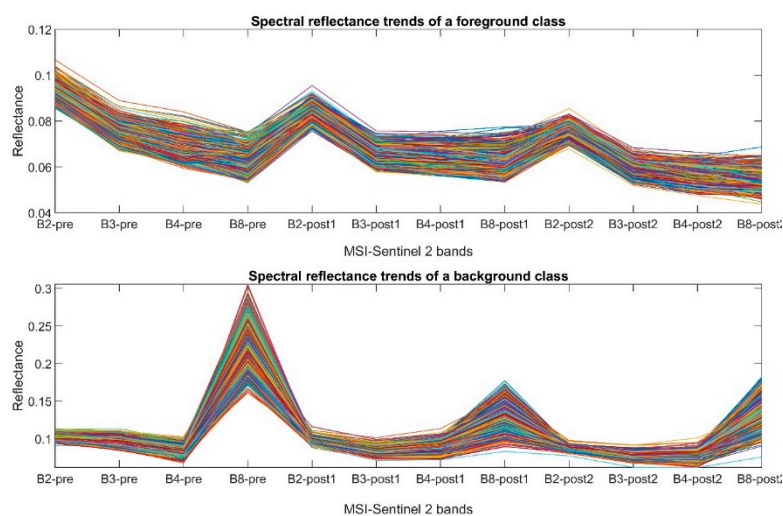


Figure 2. Difference between background (BG) and foreground (FG) pixels spectral reflectance trends over pre- and post- MSI Sentinel-2 data. Trends of pixels belonging to a FG class (up) and trends of the pixels belonging to a BG class (down) are shown. Different colored lines correspond to the pixels belonging to the FG class (up) and BG class (down).

Generally speaking, pixels inside a cluster not belonging to the recent lava flow have similar spectral responses over the pre- and post-eruptive days, while pixels inside a cluster belonging to the lava flow have different spectral responses over the pre- and post-eruptive days due to the fact that their reflectance decreases [72]. These differences can be caught from remote sensors when images are acquired under the same conditions with negligible differences in the atmospheric and environmental conditions.

As classification method, we used the k-medoids unsupervised clustering technique, which is applied to the pre-processed input data [77]. The k-medoids algorithm partitions data in groups to minimize the distance between points in each cluster and the pixel iteratively identified as the cluster center. Here, the correlation distance is adopted as a measure of similarity and is defined as one minus the sample correlation between points (treated as sequences of values). The number of clusters n is set a-priori after a trial and error procedure. Thus, each cluster will be made by highly correlated pixels resulting in a 2D map made by n clusters. The k-medoids map is built using only Sentinel 2-MSI images, without any knowledge about the real lava flow.

At this point, pixels with similar trends are grouped together and consequently any pixel inside each cluster is overall representative of the cluster itself. Unfortunately, atmospheric and environmental conditions do not allow to uniquely classify each of the cluster as belonging or not to the lava flow. Snow, clouds, and shaded and bright areas prevent using the correlation distance as the only metrics

to classify newly lava flow pixels. For instance, under certain light conditions, older and newer lava flow pixels may manifest similar trends, thus belonging to the same cluster, although not belonging to the same class. This suggests that the relationship between the input data and the output requires a more complex modelling. As a consequence, a nonlinear BNN was designed to learn how to discriminate recent lava flow pixels from both the older lava flow and the background in non-ideal condition. The BNN requires a training dataset to learn the non-linear relationship among the input and target variables. To select a representative training dataset, three pixels for each of the n clusters have to be manually labelled to create the BNN input and target. In particular, some of the pixels characterized by clouds, snow or shaded area are given as training points. The number of the selected pixels is far less than the full dataset size (less than 0.2%), but sufficient to take into account the main trends characterizing the input signals. The remaining larger portion of pixels is used to test the BNN. The BNN updates the weight and bias values according to Levenberg-Marquardt optimization minimizing a combination of squared errors and weights. Then, it determines the correct combination so as to produce a network that generalizes well. The BNN architecture consists of three layers. The standard structure that is used for neural network in pattern recognition applications is a two-layer feedforward network, with a sigmoid transfer function in the hidden layer, and a softmax transfer function in the output layer [78]. In particular, the softmax function is a normalized exponential function taking N-dimensional input and producing an N-dimensional output in the range (0, 1) whose values follow a probability distribution, i.e., their sum is 1. The sigmoid function is a monotonic S-shaped function taking an N-dimensional input and squashing the N-dimensional output in the range (0, 1) and their sum along classes is not 1 [78].

The first layer (input) has as many nodes as the input parameters (in our case, 13). The last layer (output) has two nodes, indicating the classes “recent lava flow field” (foreground) and “outside of the recent lava flow field” (background), with possible values 0 (not belonging to the class) and 1 (belonging to the class); the output layer nodes use a softmax activation function.

A single hidden layer is interposed between the input and output layers, composed of 10 neurons with a sigmoid activation function.

During the training phase, three pixels for each cluster are manually labelled to guide the following BNN training. We considered three pixels per class because they are enough to get satisfactory performance while minimizing a priori-knowledge, i.e., number of pixels to label. In particular, the three pixels closer to the medoid of each cluster are automatically selected for labelling; however, if cloudy/snowy/plume pixels are present, the expert should override the automatic choice, and label at least one of these pixels for each affected cluster, in order to avoid misclassifications. Thus, the BNN training dataset is made by three pixels for each of the n clusters, resulting in a $3n \times 13$ BNN input matrix. The target BNN array is $3n \times 2$, where each target pixel has value 0 or 1 for each of the background (outside of the lava flow) and foreground (inside the lava flow) classes, depending on the binary choice from the expert. Since the number of training pixels belonging to the lava flow is generally smaller than the number of training pixels outside of the flow, the user only has to identify the foreground pixels and the others are automatically labeled as background pixels.

Applied to an image, the BNN will produce as output an $(N \times M) \times 2$ array with the classification of each pixel. From this, we generate an $N \times M$ matrix with value 0 for pixels that are classified as background, and 1 for pixels that are classified as foreground (belonging to the “recent lava flow field” class). A final post-processing stage removes small isolated groups of pixels from the foreground of the 2D binary map. We assume that during an eruption, new lava will occupy a contiguous area within the flow field. In image processing, this operation is called image opening and it allows filtering out morphological noise, i.e., connected components having less than a certain number of pixels. Here, the connectivity is set to 4 and the object dimension to remove is set to less than 10 pixels.

The workflow leading from the input data to the mapping of cooling lava flow fields is summarized in Figure 3. The entire code has been implemented in the MATLAB 2019a environment.

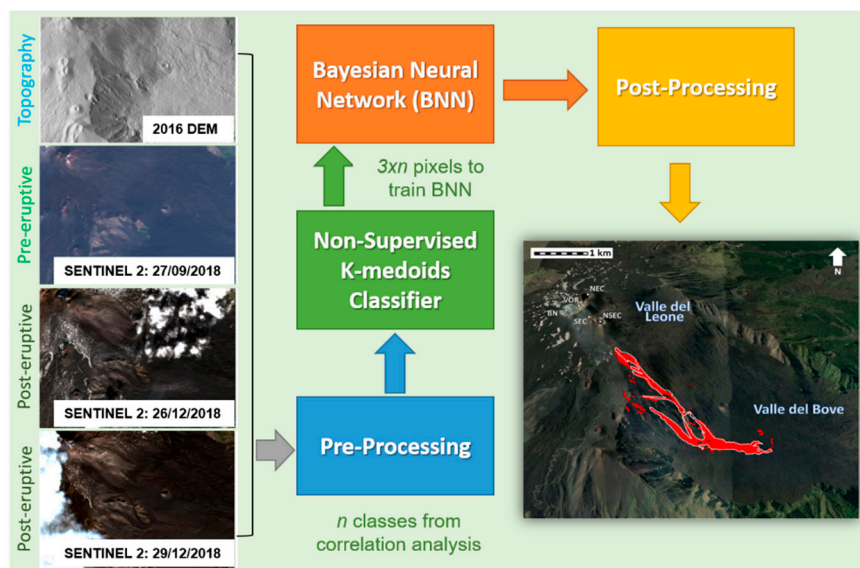


Figure 3. The workflow adopted to map lava flows using the MSI Sentinel-2 data and DEM information. The input data are firstly pre-processed and given as input to the k-medoids unsupervised clustering; then n pixels for each class are used to train the BNN. The output of the BNN is post-processed by opening the resulting image providing the areal extent of lava flow.

3. Results

3.1. Case Study: February–April 2017

The eruptive activity at Mount Etna was very intensive in the first half of 2017. It started at the end of February 2017, when lava fountains took place at the summit craters, and continued until the end of April 2017, when discontinuous lava emission formed a long, complex lava flow field in the upper south flank of the volcano [79]. In order to investigate this event, Sentinel-2 data was acquired on 9 July 2016 (have been used as pre-eruptive image, while the ones acquired on 30 April 2017 and 8 May 2017 as post-eruptive images). The area of interest was restricted to the region where the eruptive activity took place. In particular, each of the 10 m spatial resolution bands was zoomed to smaller areas of 321×333 pixels. In Figure 4, the 2016 DEM [33] and RGB composite from Sentinel-2 MSI data (Red—Band 4, Green—Band 3, Blue—Band 2) of the pre- and post-eruptive images are shown.

In order to build the input dataset, each pixel is considered as characterized by 13 components, namely bands 2, 3, 4, 8 of day 9 July 2016; bands 2, 3, 4, 8 of day 30 April 2017; bands 2, 3, 4, 8 of day 8 May 2017, and DEM. The k-medoids stage receives as input the $106,893 \times 13$ matrix, and it clusters the 106,893 pixels in 50 classes depending on their correlation distances. For the training set, 150 pixels have to be labelled (as described in Section 2.2), and it is noteworthy that, in this case, only 17 pixels out of 150 training pixels belong to the lava flow field, so our results have been obtained labelling only 0.016% of the full dataset size to train our model. In order to test the trained BNN, the remaining $106,743 \times 13$ pixels are used, producing as a result the output map. Finally, the post-processing step is performed on the output, removing some noisy isolated pixels. The final lava flow map after the last post-processing step is shown in Figure 5 together with the contour of the real observed lava flow manually retrieved from multi-view PlanetScope images (four bands: Blue, Green, Red plus Near Infrared with a ground sampling distance of ~ 3.7 m).

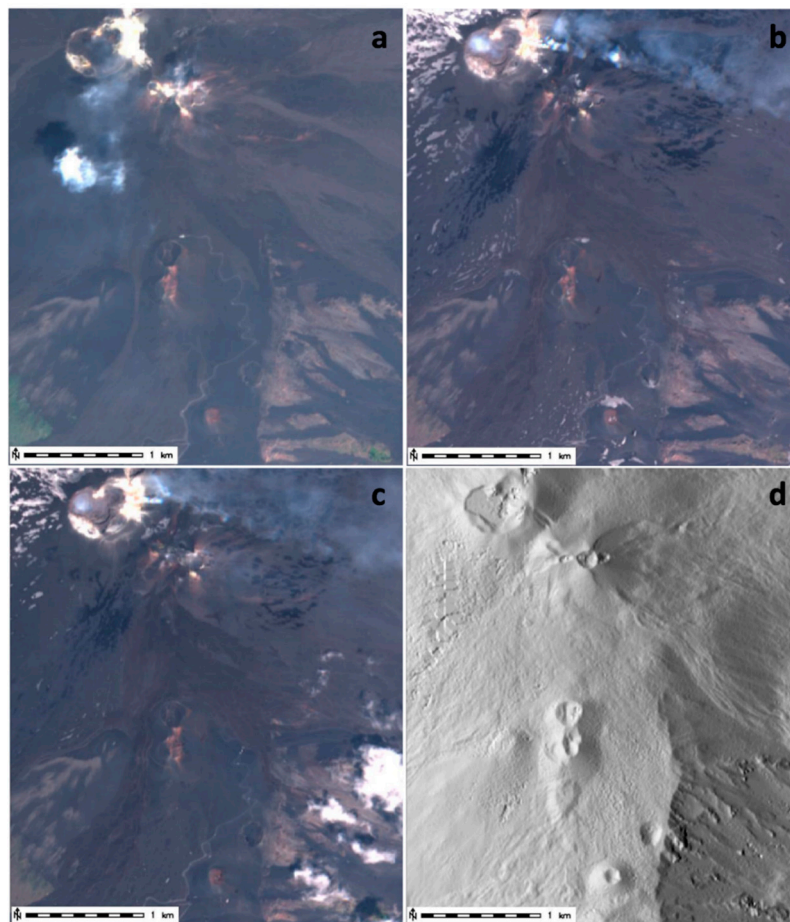


Figure 4. RGB composition from Sentinel-2 MSI data (Red—Band 4, Green—Band 3, Blue—Band 2) of the pre-eruptive area 9 July 2016 (a), post-eruptive area 30 April 2017 (b) and 8 May 2017 (c) and DEM 2016 (d) restricted to the lava flow region.

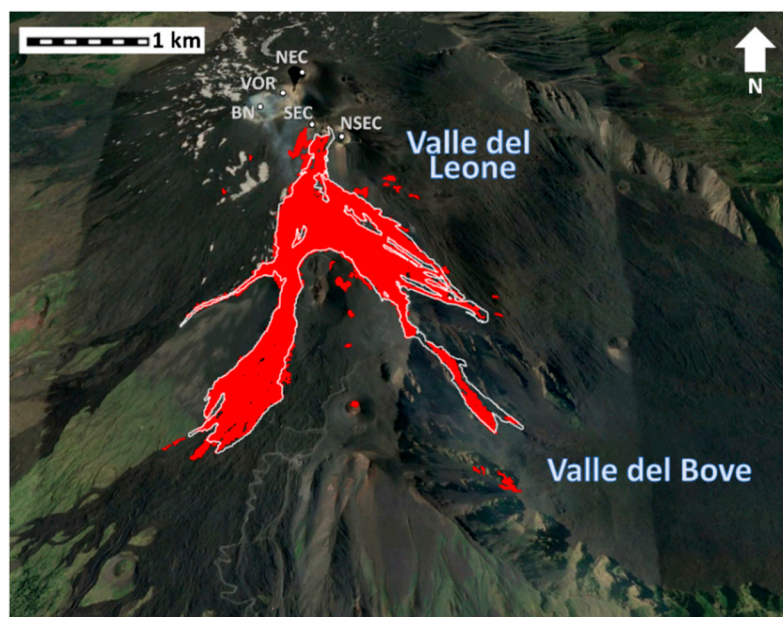


Figure 5. Lava flow map resulting from the BNN and the post-processing stages (red) and the contour of the real lava flow (white) observed during the 2017 Etna eruption.

3.2. Case of Study: August 2018

On the 23 August, a new eruption of Mt Etna started with strombolian explosions from the saddle cone located between the South-East Crater (SEC) and the New South-East Crater (NSEC). Immediately after, a tiny lava flow was emitted by the NSEC towards Valle del Bove, while a further lava overflow was emitted by the saddle cone towards the north direction in the Valle del Leone. On the 27 August, the northernmost lava flow was cooling while a new lava flow was emitted from the NSEC towards Valle del Bove [22]. The two lava flows have been processed separately, taking into account two different sets of images due to the fact that in the best images for the northern lava flow, the southernmost flow was hidden by clouds/plumes. The closest post-eruptive MSI data available and not affected by clouds are the ones recorded on 28 August 2018 and 12 September 2018 for the northern lava flow and 12 September 2018 and 27 September 2018 for the southern lava flow. The MSI data recorded on 3 August 2017 is used as a pre-eruptive image. The areas of interest for each flow are zoomed to the regions where each of the flow is emplaced. In particular, each of the 10 m spatial resolution bands image is 70×216 pixels, including either the northern or the southern lava flow. The k-medoids stage receives as input a $15,120 \times 13$ matrix for each case, producing again 50 clusters for each flow. After manual labelling of 150 pixels per flow, training and applying the BNN to the remaining $14,970 \times 13$ pixels, and post-processing the result, we obtain the map shown in Figure 6. It is worth to mention that our results have been obtained labelling only 0.17% and 0.1% of the full datasets size as belonging to the lava flow for the northern and southern lava flows, respectively.

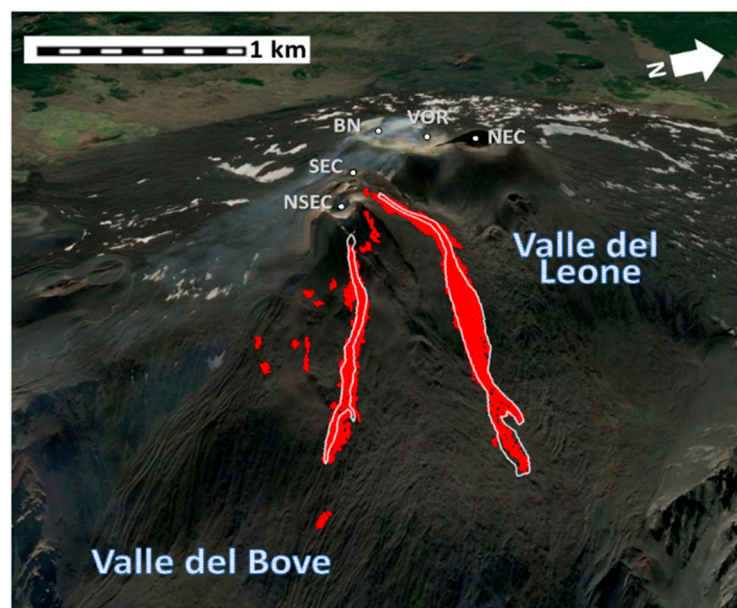


Figure 6. Lava flow map resulting from the BNN and the post-processing stages (red) and the contour of the real lava flow (white) observed during the Etna eruption occurred in August 2018. The northern flow is the one emitted on 24 August, while the southern one was erupted on 27 August.

3.3. Case Study: December 2018

Mount Etna volcano erupted again between 24 and 27 December 2018 from a fissure that opened on the high south-eastern flank, generating a lava flow spreading in Valle del Bove. The closest pre-eruptive and post-eruptive MSI data available and not affected by clouds are the ones recorded on 27 September 2018 (pre) and 26–29 December 2018 (post), respectively. The size of the area of interest is zoomed to the region of size 266×401 pixels, i.e., the input matrix is $67,084 \times 13$. In this case, one post-eruptive dataset was recorded when the lava eruption was still taking place, and the hot portion of the lava flow is easily identified with a simple threshold on MSI Band 12. Therefore,

we build our model with only the cooling lava flow portion; then, in order to get the whole lava flow field, we merge our results with the hot lava flow portion resulting from the thresholding. Filtering out the hot lava flow pixels, a $53,443 \times 13$ input matrix is given as input to the k-medoids stage that clusters the pixels in 50 classes, like in the other cases. For the training stage, only 15 of the 150 training pixels belong to the lava flow field, i.e., only 0.028% of the full dataset is labelled as belonging to the cooling lava flow. In order to test the trained BNN, the remaining $53,293 \times 13$ pixels are used. After the post-processing step is performed, the hot lava flow portion is added to the cooling lava flow previously obtained, producing as a result the 2D map shown in Figure 7.

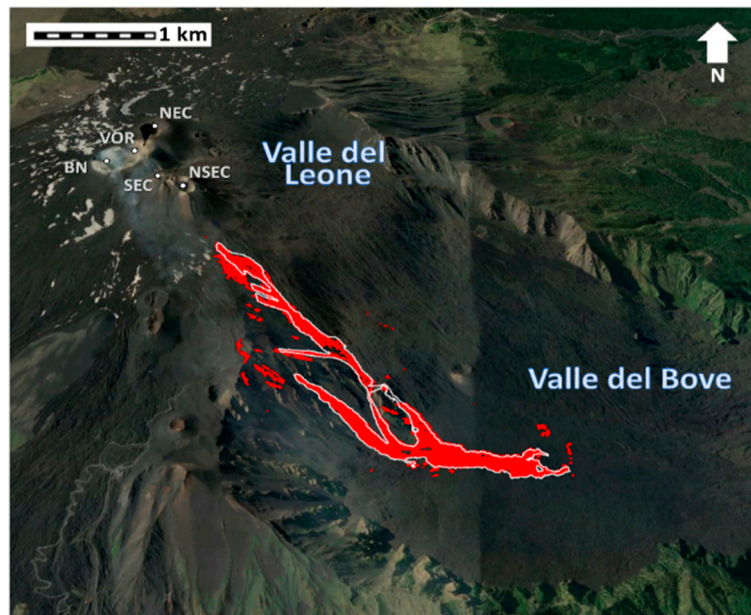


Figure 7. Lava flow map resulting from the BNN and the post-processing stages (red) and the contour of the real lava flow (white) observed during the Etna eruption that occurred in December 2018.

4. Discussion

In order to assess the accuracy of the maps produced by machine learning techniques, we compare them to the maps of actual lava flow fields of the three investigated Etna eruptions manually retrieved from multi-view PlanetScope images (four bands: Blue, Green, Red plus Near Infrared with a ground sampling distance of ~ 3.7 m). To determine the robustness of our results, we computed three different performance indices, which have been extensively used to quantify the goodness of fit between real and simulated lava flows [62,80–82]:

- **accuracy** (ACC) = $\sqrt{\frac{A(\text{test} \cap \text{ref})}{A(\text{test} \cup \text{ref})}}$
- **precision** (also known as the *positive predictive value*, PPV) = $\sqrt{\frac{A(\text{test} \cap \text{ref})}{A(\text{test})}}$
- **sensitivity** (also known as the *true positive rate*, TPR) = $\sqrt{\frac{A(\text{test} \cap \text{ref})}{A(\text{ref})}}$

where $A(\text{test})$ and $A(\text{ref})$ are the testing and reference areas, respectively.

A comparison between the ACC , PPV and TPR provides insights on how the testing placements change compared to the actual areas. Specifically, the testing area underestimates the actual one if PPV is higher than ACC , while it overestimates if TPR is greater than ACC [83,84].

Table 1 shows the areal extent of lava flows for the investigated eruptions extracted from Sentinel-2 MSI data (BNN), ground-based measurements (GROUND), and PlanetScope images (REAL). Results for ACC , PPV and TPR calculated for BNN and GROUND (as testing) and REAL (as reference) are also reported.

Table 1. Comparison between lava flows extracted from Sentinel-2 MSI data (BNN), ground-based measurements (GROUND), and PlanetScope images (REAL). For each event, the areal extents and the results for the three performance indices ACC, PPV and TPR are reported. Ground-based areas were extracted from the weekly INGV bulletins (available at <http://www.ct.ingv.it/it/rapporti/multidisciplinari>) and from the final report of the DPC-INGV 2016 agreement All. B2 Task D4. Real areas were retrieved from PlanetScope images acquired on 7 May 2017, 28 August 2018 and 29 December 2018.

Eruption Date	Area [km ²]			ACC		PPV		TPR	
	REAL	BNN	GROUND	BNN	GROUND	BNN	GROUND	BNN	GROUND
February–April 2017	2.03	1.99	1.45	0.88	0.73	0.88	0.83	0.86	0.60
August 2018	0.21	0.28	0.38	0.73	0.52	0.60	0.33	0.81	0.58
December 2018	0.88	0.94	0.73	0.83	0.58	0.79	0.56	0.84	0.46

BNN mapping is more accurate than the ground-based one and fully in agreement with the real lava flows in all the presented cases of study. Indeed, the values for ACC, PPV and TPR are always higher than 0.60 for all the three case studies, meaning that the real lava flow field is always well reproduced.

The best fits (ACC = PPV = 0.88, TPR = 0.86) are obtained for the lava flow of February–April 2017, while the worst case is August 2018 (ACC = 0.73, PPV = 0.60, TPR = 0.81). The performances get worse when the closest available images are recorded weeks after the lava eruption ends, thus reducing the information available to infer the lava flow map. In fact, after several days, it gets harder to distinguish older and newer lava flows. For instance, this happened for the lava flow of 27 August 2018, when one of the clouds and snow-free Sentinel 2-MSI datasets used as post-eruptive images are recorded nearly 45 and 30 days later, respectively. On the other hand, for April 2017, the farthest image used as post-eruptive image is recorded nine days after the volcanic eruption ends, thus leading to good performances; similarly, for the northern lava flow of the August 2018 case study.

Another major factor that can reduce the BNN performance is the presence of ice, snow, atmospheric clouds, ash and/or tephra plumes. For example, the images we used for December 2018 were affected by clouds, plumes/ash, and snow, resulting in noisy pixels that represented a source of error for our classifier. The combination of all these factors can increase uncertainty, worsening overall performance.

It is worth noting that different lava flow morphologies [85–88] do exist. In the cases under investigation, i.e., Etna lava flows, the morphology of the lava is primarily ‘a’ā, but some portions can show pahoehoe features. The Machine Learning algorithm aiming to discriminate recent lava flows from both older lava flows and background is able to manage differences in morphologies during the k-medoids clustering stage, where pixels with similar features, i.e., similar morphology lava flow portions, are grouped together. We have successfully applied our automatic procedure only to Etna, so further tests with other volcanoes showing different kind of lavas with different morphologies are necessary to examine its robustness and reliability. The morphologies’ differences, together with the changing environmental and atmospheric conditions, lead to the need to train the BNN for each case study rather than just once.

The existing methods have limitations, such as the difficulty to handle the big extension of a lava flow with either aerial or ground instruments, while avoiding hazardous locations. Moreover, manual outlines from satellite images is time-consuming with respect to our algorithm, whose processing can be run in a common laptop with processing time varying from 2 to 15 min, depending on the size of the lava flow. A short time is needed for labelling, because only pixels belonging to the lava flow classes are labelled for the training phase; they are far less than 150 pixels, i.e., the left ones are automatically identified as background pixels. Furthermore, sometimes human eye-perception is not precise as expected; we tested that the BNN was able to identify portions of an extended lava flow field that were not identified with a manual outline.

On the other hand, the BNN based on a 10-m spatial resolution data enlarges the actual lava flow field because of MSI instrumental limits. Furthermore, the lack of at least a post-eruptive dataset

close enough to the eruption ending date worsens the performance of the algorithm, as shown in the southern lava flow of the August 2018 case study.

Further development to improve the overall performance could enable the clustering stage to set the number of clusters automatically. Moreover, the availability of a far bigger dataset could allow the formation of a unique BNN, trained just once and applicable to all the other cases.

5. Conclusions

We introduced a new machine-learning approach to map recent lava flows that exploits the high spatial resolution and freely available information coming from Sentinel 2-MSI channels. Our approach relies on a k-medoids unsupervised classifier, able to separate the data points in n different clusters, depending on the correlation measure among the pixels belonging to the area of interest. Although this method allows to group pixels having similar trends, it is not able to properly discriminate pixels belonging to recent lava flow and pixels not belonging to it. Thus, a second step relying on a Bayesian neural network is performed to map recent lava flows.

Three recent effusive eruptions at Mount Etna were investigated, namely February–April 2017, August 2018 and December 2018. The results show that the BNN outcomes are in good agreement with the target in all the three eruptions. It is worth noting that the reference lava flow maps that have been used to validate our approach have been manually produced by using PlanetScope data; these images are very detailed, but not freely available and quite expensive.

Even though some isolated pixels are wrongly classified as belonging to the lava flow, our machine-learning approach is able to correctly identify the main lava flow body by only knowing at most 0.02% of the lava flow field. In fact, very few labelled pixels are sufficient to get a coarse lava flow map from the BNN, but the performance of this approach can further be improved by increasing the number of labelled pixels. Overall, our BNN classifier produces excellent results, especially when the available images are recorded within few weeks of the end of the lava emission; after this period of time, the performances get worse. Although the performance is largely improved by using more pixels per class, this would mean knowing a-priori more points belonging to the lava flow.

Lava-flow maps produced adopting this approach can be used to facilitate field mapping, giving insights into emplacement processes, and improving the monitoring and assessment of lava flow hazards. It is noteworthy that by using this technique, only the geo-located and calibrated 10-m Sentinel 2-MSI images and a few labelled pixels are needed to map lava flows with 10 m spatial resolution. Furthermore, although MATLAB enables the use of GPUs to accelerate time-processing, most of the processing can be run on a common laptop with processing time varying from 2 min to 15 min, depending on the size of the lava flow, thus representing a valuable time-saving mapping tool.

This method has been applied to Mount Etna, but our machine-learning approach has been designed to be applicable to other volcanic areas.

Author Contributions: Conceptualization, C.C. and G.G.; Data curation, G.G.; Funding acquisition, A.H. and C.D.N.; Methodology, C.C. and G.B.; Software, C.C.; Supervision, C.D.N.; Validation, A.C.; Writing—Original draft, C.C., G.G. and A.C.; Writing—Review & Editing, G.B. and C.D.N.

Funding: This research was partially funded by the ATHOS Research Programme.

Acknowledgments: This work was developed within the framework of the Laboratory of Technologies for Volcanology (TecnoLab) at INGV in Catania (Italy). Sentinel-2 images are courtesy of the Copernicus Open Access Hub (<https://scihub.copernicus.eu>). Pléiades data were available through the Space Volcano Observatory with Pléiades (SVOP) project coordinated by Pierre Briole (http://volcano.terre.fr/svo_projects). We would like to thank Planet Labs, Inc. for providing the PlanetScope imagery through the Education and Research Program. Ground-based lava flow areas were extracted from the weekly INGV bulletins (http://www.ct.ingv.it/it/rapporti/multidisciplinari/doc_view/9951-bollettino-settimanale-sul-monitoraggio-vulcanico-geochimico-e-sismico-del-vulcano-etna-04-09-2018.html for August 2018 and http://www.ct.ingv.it/it/rapporti/multidisciplinari/doc_download/10009-bollettino-settimanale-sul-monitoraggio-vulcanico-geochimico-e-sismico-del-vulcano-etna-01-01-2019.html for December 2018) and from the final report of the DPC-INGV 2016 agreement All. B2 Task D4 (for February–April 2017). We thank the Editor and three anonymous reviewers for their constructive and supportive comments that helped to improve the manuscript.

Conflicts of Interest: The authors declare no conflict of interest.

References

1. Del Negro, C.; Cappello, A.; Neri, M.; Bilotta, G.; Hérault, A.; Ganci, G. Etna flank lava flows between 1610 and 2008. *PANGAEA* **2013**. [[CrossRef](#)]
2. Cappello, A.; Geshi, N.; Neri, M.; Del Negro, C. Lava flow hazards-An impending threat at Miyakejima volcano, Japan. *J. Volcanol. Geotherm. Res.* **2015**, *308*, 1–9. [[CrossRef](#)]
3. Cappello, A.; Zanon, V.; Del Negro, C.; Ferreira, T.J.L.; Queiroz, M.G.P.S. Exploring lava-flow hazards at Pico Island, Azores Archipelago (Portugal). *Terra Nova* **2015**, *27*, 156–161. [[CrossRef](#)]
4. Pedrazzi, D.; Cappello, A.; Zanon, V.; Del Negro, C. Impact of effusive eruptions from the Eguas-Carvao fissure system, Sao Miguel Island, Azores Archipelago (Portugal). *J. Volcanol. Geotherm. Res.* **2015**, *291*, 1–13. [[CrossRef](#)]
5. Pedersen, G.B.M.; Höskuldsson, A.; Dürig, T.; Thordarson, T.; Jónsdóttir, I.; Riishuus, M.S.; Óskarsson, B.V.; Dumont, S.; Magnusson, E.; Gudmundsson, M.T.; et al. Lava field evolution and emplacement dynamics of the 2014–2015 basaltic fissure eruption at Holuhraun, Iceland. *J. Volcanol. Geotherm. Res.* **2017**, *340*, 155–169. [[CrossRef](#)]
6. Del Negro, C.; Cappello, A.; Ganci, G. Quantifying lava flow hazards in response to effusive eruption. *Geol. Soc. Am. Bull.* **2016**, *128*, 752–763. [[CrossRef](#)]
7. Carr, B.B.; Clarke, A.B.; Arrowsmith, J.R.; Vanderkluysen, L.; Dhanu, B.E. The emplacement of the active lava flow at Sinabung Volcano, Sumatra, Indonesia, documented by structure-from-motion photogrammetry. *J. Volcanol. Geotherm. Res.* **2018**. [[CrossRef](#)]
8. James, M.R.; Pinkerton, H.; Applegarth, L.J. Detecting the development of active lava flow fields with a very-long-range terrestrial laser scanner and thermal imagery. *Geophys. Res. Lett.* **2009**, *36*, L22305. [[CrossRef](#)]
9. James, M.R.; Pinkerton, H.; Robson, S. Image-based measurement of flux variation in distal regions of active lava flows. *Geochem. Geophys. Geosyst.* **2007**, *8*, Q03006. [[CrossRef](#)]
10. Vicari, A.; Ganci, G.; Behncke, B.; Cappello, A.; Neri, M.; Del Negro, C. Near-real-time forecasting of lava flow hazards during the 12–13 January 2011 Etna eruption. *Geophys. Res. Lett.* **2011**, *38*, L13317. [[CrossRef](#)]
11. Stevens, N.F.; Wadge, G.; Murray, J.B. Lava flow volume and morphology from digitised contour maps: A case study at Mount Etna, Sicily. *Geomorphology* **1999**, *28*, 251–261. [[CrossRef](#)]
12. Cashman, K.V.; Sparks, R.S.J. How volcanoes work: A 25 year perspective. *Geol. Soc. Am. Bull.* **2013**, *125*, 664–690. [[CrossRef](#)]
13. Turner, N.R.; Perroy, R.L.; Hon, K. Lava flow hazard prediction and monitoring with UAS: A case study from the 2014–2015 Pāhoa lava flow crisis, Hawai'i. *J. Appl. Volcanol.* **2017**, *6*, 17. [[CrossRef](#)]
14. Huang, H.; Long, J.; Yi, W.; Yi, Q.; Zhang, G.; Lei, B. A method for using unmanned aerial vehicles for emergency investigation of single geo-hazards and sample applications of this method. *Nat. Hazards Earth Syst. Sci.* **2017**, *17*, 1961–1979. [[CrossRef](#)]
15. Ganci, G.; Cappello, A.; Bilotta, G.; Hérault, A.; Zago, V.; Del Negro, C. Mapping Volcanic Deposits of the 2011–2015 Etna Eruptive Events Using Satellite Remote Sensing. *Front. Earth Sci.* **2018**, *6*, 83. [[CrossRef](#)]
16. Kauahikaua, J.; Margruter, S.; Lockwood, J.; Trusdell, F. *Applications of GIS to the Estimation of Lava Flow Hazards on Mauna Loa Volcano, Hawai'i*; Washington DC American Geophysical Union Geophysical Monograph Series; American Geophysical Union: Washington, DC, USA, 1995; Volume 92, pp. 315–325.
17. Calvari, S.; Neri, M.; Pinkerton, H. Effusion rate estimations during the 1999 summit eruption on Mount Etna, and growth of two distinct lava flow fields. *J. Volcanol. Geotherm. Res.* **2003**, *119*, 107–123. [[CrossRef](#)]
18. Abrams, M.; Abbott, E.; Kahle, A. Combined use of visible, reflected infrared, and thermal infrared images for mapping Hawaiian lava flows. *J. Geophys. Res.* **1991**, *96*, 475–484. [[CrossRef](#)]
19. Blackett, M. Review of the utility of infrared remote sensing for detecting and monitoring volcanic activity with the case study of shortwave infrared data for Lascar Volcano from 2001–2005. *Geol. Soc. Lond. Spec. Publ.* **2013**, *380*, 107–135. [[CrossRef](#)]

20. Bonaccorso, A.; Caltabiano, T.; Currenti, G.; Del Negro, C.; Gambino, S.; Ganci, G.; Giammanco, S.; Greco, F.; Pistorio, A.; Salerno, G.; et al. Dynamics of a lava fountain revealed by geophysical, geochemical and thermal satellite measurements: The case of the 10 April 2011 Mt. Etna eruption. *Geophys. Res. Lett.* **2011**, *38*, L24307. [[CrossRef](#)]
21. Kervyn, M.; Kervyn, F.; Goossens, R.; Rowland, S.K.; Ernst, G.G.J. Mapping volcanic terrain using high-resolution and 3D satellite remote sensing. *Geol. Soc. Am. Bull.* **2007**, *283*, 5–30. [[CrossRef](#)]
22. Ganci, G.; Cappello, A.; Zago, V.; Bilotta, G.; Herault, A.; Del Negro, C. 3D Lava flow mapping of the 17–25 May 2016 Etna eruption using tri-stereo optical satellite data. *Ann. Geophys.* **2018**. [[CrossRef](#)]
23. Bonaccorso, A.; Calvari, S.; Currenti, G.; Del Negro, C.; Ganci, G.; Linde, A.; Napoli, R.; Sacks, S.; Sicali, A. From source to surface: Dynamics of Etna’s lava fountains investigated by continuous strain, magnetic, ground and satellite thermal data. *Bull. Volcanol.* **2013**, *75*, 690. [[CrossRef](#)]
24. Amici, S.; Piscini, A.; Neri, M. Reflectance Spectra Measurements of Mt. Etna: A Comparison with Multispectral / Hyperspectral Satellite. *Adv. Remote Sens.* **2014**, *3*, 235–245. [[CrossRef](#)]
25. Ganci, G.; Bilotta, G.; Cappello, A.; Herault, A.; Del Negro, C. HOTSAT: A multiplatform system for the thermal monitoring of volcanic activity using satellite data. *Geolog. Soc. Lond. Spec. Publ.* **2016**, *426*, 207–221. [[CrossRef](#)]
26. Corradino, C.; Ganci, G.; Bilotta, G.; Cappello, A.; Del Negro, C.; Fortuna, L. Smart Decision Support Systems for Volcanic Applications. *Energies* **2019**, *12*, 1216. [[CrossRef](#)]
27. Dietterich, H.R.; Downs, D.T.; Stelten, M.E.; Zahran, H. Reconstructing lava flow emplacement histories with rheological and morphological analyses: The Harrat Rahat volcanic field, Kingdom of Saudi Arabia. *Bull. Volcanol.* **2018**, *80*, 85. [[CrossRef](#)]
28. Kubanek, J.; Richardson, J.A.; Charbonnier, S.J.; Connor, L.J. Lava flow mapping and volume calculations for the 2012–2013 Tolbachik, Kamchatka, fissure eruption using bistatic TanDEM-X InSAR. *Bull. Volcanol.* **2015**, *77*, 106. [[CrossRef](#)]
29. Lu, Z.; Fielding, E.; Patrick, M.R.; Trautwein, C.M. Estimating lava volume by precision combination of multiple baseline spaceborne and airborne interferometric synthetic aperture radar: The 1997 eruption of Okmok volcano, Alaska. *IEEE Trans. Geosci. Remote Sens.* **2003**, *41*, 1428–1436. [[CrossRef](#)]
30. Zebker, H.A.; Rosen, P.; Hensley, S.; Mouginiis-Mark, P.J. Analysis of active lava flows on Kilauea volcano, Hawaii, using SIR-C radar correlation measurements. *Geology* **1996**, *24*, 495–498. [[CrossRef](#)]
31. Dietterich, H.R.; Poland, M.P.; Schmidt, D.A.; Cashman, K.V.; Sherrod, D.R.; Espinosa, A.T. Tracking lava flow emplacement on the east rift zone of Kilauea, Hawai’i, with synthetic aperture radar coherence. *Geochem. Geoph. Geosy.* **2012**, *13*. [[CrossRef](#)]
32. Bonny, E.; Thordarson, T.; Wright, R.; Höskuldsson, A.; Jónsdóttir, I. The volume of lava erupted during the 2014 to 2015 eruption at Holuhraun, Iceland: A comparison between satellite- and ground-based measurements. *J. Geophys. Res. Solid Earth* **2018**, *123*, 5412–5426. [[CrossRef](#)]
33. Head, E.M.; Maclean, A.L.; Carn, S.A. Mapping lava flows from Nyamuragira volcano (1967–2011) with satellite data and automated classification methods. *Nat. Hazards Risk* **2013**, *4*, 119–144. [[CrossRef](#)]
34. Lu, Z.; Rykhus, R.; Masterlark, T.; Dean, K.G. Mapping recent lava flows at Westdahl Volcano, Alaska, using radar and optical satellite imagery. *Remote Sens. Environ.* **2004**, *91*, 345–353. [[CrossRef](#)]
35. Bagnardi, M.; González, P.J.; Hooper, A. High-resolution digital elevation model from tri-stereo Pléiades-1 satellite imagery for lava flow volume estimates at Fogo Volcano. *Geophys. Res. Lett.* **2016**, *43*, 6267–6275. [[CrossRef](#)]
36. Albino, F.; Smets, B.; d’Oreye, N.; Kervyn, F. High-resolution TanDEM-X DEM: An accurate method to estimate lava flow volumes at Nyamulagira volcano (D. R. Congo). *J. Geophys. Res. Solid Earth* **2015**, *120*, 4189–4207. [[CrossRef](#)]
37. Anantrasirichai, N.; Achim, A.; Morgan, J.E.; Erchova, I.; Nicholson, L. SVM-based texture classification in optical coherence tomography. In Proceedings of the IEEE 10th International Symposium on Biomedical Imaging, San Francisco, CA, USA, 7–11 April 2013; pp. 1332–1335. [[CrossRef](#)]
38. Anantrasirichai, N.; Biggs, J.; Albino, F.; Hill, P.; Bull, D. Application of Machine Learning to Classification of Volcanic Deformation in Routinely Generated InSAR Data. *J. Geophys. Res. Solid Earth* **2018**, *123*, 6592–6606. [[CrossRef](#)]

39. Chang, N.B.; Bai, K.; Chen, C.F. Integrating multisensor satellite data merging and image reconstruction in support of machine learning for better water quality management. *J. Environ. Manag.* **2017**, *201*, 227–240. [[CrossRef](#)]
40. Chang, C.C.; Lin, C.J. LIBSVM: A library for support vector machines. *ACM Trans. Intell. Syst. Technol.* **2011**, *2*, 27. [[CrossRef](#)]
41. Jeppesen, J.H.; Jacobsen, R.H.; Inceoglu, F.; Toftgaard, T.S. A cloud detection algorithm for satellite imagery based on deep learning. *Remote Sens. Environ.* **2019**, *229*, 247–259. [[CrossRef](#)]
42. Kotsiantis, S.B. Supervised machine learning: A review of classification techniques. In *Emerging Artificial Intelligence Applications in Computer Engineering: Real World AI Systems with Applications in eHealth, HCI, Information Retrieval and Pervasive Technologies*; IOS Press: Amsterdam, The Netherlands, 2007; pp. 3–24.
43. Yilmaz, I. Comparison of landslide susceptibility mapping methodologies for Koyulhisar, Turkey: Conditional probability, logistic regression, artificial neural networks, and support vector machine. *Environ. Earth Sci.* **2010**, *61*, 821–836. [[CrossRef](#)]
44. Brown, M.; Lary, D.; Vrieling, A.; Stathakis, D.; Mussa, H. Neural networks as a tool for constructing continuous NDVI time series from AVHRR and MODIS. *Int. J. Remote Sens.* **2008**, *29*, 7141–7158. [[CrossRef](#)]
45. Chen, Y.; Fan, R.; Bilal, M.; Yang, X.; Wang, J.; Li, W. Multilevel cloud detection for high-resolution remote sensing imagery using multiple convolutional neural networks. *ISPRS Int. J. Geo Inf.* **2018**, *7*, 181. [[CrossRef](#)]
46. Kadavi, P.R.; Lee, C.W. Land cover classification analysis of volcanic island in Aleutian Arc using an artificial neural network (ANN) and a support vector machine (SVM) from Landsat imagery. *Geosci. J.* **2018**, *22*, 653–665. [[CrossRef](#)]
47. Raith, S.; Vogel, E.P.; Anees, N.; Keul, C.; Güth, J.F.; Edelhoff, D.; Fischer, H. Artificial Neural Networks as a powerful numerical tool to classify specific features of a tooth based on 3D scan data. *Comput. Biol. Med.* **2017**, *80*, 65–76. [[CrossRef](#)] [[PubMed](#)]
48. Apicella, M.L.; Buscarino, A.; Corradino, C.; Fortuna, L.; Mazzitelli, G.; Xibilia, M.G. Temperature Model Identification of FTU Liquid Lithium Limiter. *IEEE Trans. Control Syst. Technol.* **2018**, *26*, 1132–1139. [[CrossRef](#)]
49. Yoshida, T.; Omatu, S. Pattern recognition with neural networks. In Proceedings of the IEEE 2000 International Geoscience and Remote Sensing Symposium. Taking the Pulse of the Planet: The Role of Remote Sensing in Managing the Environment Proceedings (Cat. No. 00CH37120), Honolulu, HI, USA, 24–28 July 2000; Volume 2, pp. 699–701.
50. Adeli, H.; Panakkat, A. A probabilistic neural network for earthquake magnitude prediction. *Neural Netw.* **2009**, *22*, 1018–1024. [[CrossRef](#)] [[PubMed](#)]
51. Erhan, D.; Bengio, Y.; Courville, A.; Manzagol, P.A.; Vincent, P.; Bengio, S. Why does unsupervised pre-training help deep learning? *J. Mach. Learn. Res.* **2010**, *11*, 625–660.
52. Gaddam, S.R.; Phoha, V.V.; Balagani, K.S. K-Means+ID3: A novel method for supervised anomaly detection by cascading K-Means clustering and ID3 decision tree learning methods. *IEEE Trans. Knowl. Data Eng.* **2007**, *19*, 345–354. [[CrossRef](#)]
53. Tien Bui, D.; Tuan, T.A.; Hoang, N.D.; Thanh, N.Q.; Nguyen, D.B.; Van Liem, N.; Pradhan, B. Spatial prediction of rainfall-induced landslides for the Lao Cai area (Vietnam) using a hybrid intelligent approach of least squares support vector machines inference model and artificial bee colony optimization. *Landslides* **2017**, *14*, 447–458. [[CrossRef](#)]
54. Handayani, A.N.; Lathifah, N.; Herwanto, H.W.; Asmara, R.S.; Arai, K. Neural Network Bayesian Regularization Backpropagation to Solve Inverse Kinematics on Planar Manipulator. In Proceedings of the 2018 Joint 7th International Conference on Informatics, Electronics & Vision (ICIEV) and 2018 2nd International Conference on Imaging, Vision & Pattern Recognition (ICIVPR), Kitakyushu, Japan, 25–29 June 2018; pp. 99–104.
55. Cappello, A.; Bilotta, G.; Neri, M.; Del Negro, C. Probabilistic modeling of future volcanic eruptions at Mount Etna. *J. Geophys. Res. Solid Earth* **2013**, *118*, 1925–1935. [[CrossRef](#)]
56. Acocella, V.; Neri, M.; Behncke, B.; Bonforte, A.; Del Negro, C.; Ganci, G. Why does a mature volcano need new vents? the case of the new southeast crater at etna. *Front. Earth Sci.* **2016**, *4*, 67. [[CrossRef](#)]
57. Neri, M.; Acocella, V.; Behncke, B.; Maiolino, V.; Ursino, A.; Velardita, R. Contrasting triggering mechanisms of the 2001 and 2002–2003 eruptions of Mount Etna (Italy). *J. Volcanol. Geotherm. Res.* **2005**, *144*, 235–255. [[CrossRef](#)]

58. Behncke, B.; Fornaciai, A.; Neri, M.; Favalli, M.; Ganci, G.; Mazzarini, F. Lidar surveys reveal eruptive volumes and rates at Etna, 2007–2010. *Geophys. Res. Lett.* **2016**, *43*, 4270–4278. [[CrossRef](#)]
59. Ganci, G.; Vicari, A.; Cappello, A.; Del Negro, C. An emergent strategy for volcano hazard assessment: From thermal satellite monitoring to lava flow modeling. *Remote Sens. Environ.* **2012**, *119*, 197–207. [[CrossRef](#)]
60. Ganci, G.; Cappello, A.; Bilotta, G.; Corradino, C.; Del Negro, C. Satellite-Based Reconstruction of the Volcanic Deposits during the December 2015 Etna Eruption. *Data* **2019**, *4*, 120. [[CrossRef](#)]
61. Cappello, A.; Ganci, G.; Bilotta, G.; Corradino, C.; Herault, A.; Del Negro, C. Changing eruptive styles at the South-East Crater of Mount Etna: Implications for assessing lava flow hazards. *Front. Earth Sci.* **2019**, *7*, 213. [[CrossRef](#)]
62. Del Negro, C.; Cappello, A.; Neri, M.; Bilotta, G.; Herault, A.; Ganci, G. Lava flow hazards at Mount Etna: Constraints imposed by eruptive history and numerical simulations. *Sci. Rep.* **2013**, *3*, 3493. [[CrossRef](#)]
63. Patrick, M.R.; Dehn, J.; Papp, K.R.; Lu, Z.; Dean, K.; Moxey, L.; Izbekov, P.; Guritz, R. The 1997 eruption of Okmok Volcano, Alaska: A synthesis of remotely sensed imagery. *J. Volcanol. Geoth. Res.* **2003**, *127*, 87–105. [[CrossRef](#)]
64. Pyle, D.M.; Mather, T.A.; Biggs, J. Remote sensing of volcanoes and volcanic processes: Integrating observation and modelling—introduction. *Geol. Soc. Lond. Spec. Publ.* **2013**, *380*, 1–13. [[CrossRef](#)]
65. Rogic, N.; Cappello, A.; Ferrucci, F. Role of Emissivity in Lava Flow ‘Distance-to-Run’ Estimates from Satellite-Based Volcano Monitoring. *Remote Sens.* **2019**, *11*, 662. [[CrossRef](#)]
66. Valade, S.; Ley, A.; Massimetti, F.; D’Hondt, O.; Laiolo, M.; Coppola, D.; Loibl, D.; Hellwich, O.; Walter, T.R. Towards Global Volcano Monitoring Using Multisensor Sentinel Missions and Artificial Intelligence: The MOUNTS Monitoring System. *Remote Sens.* **2019**, *11*, 1528. [[CrossRef](#)]
67. Wadge, G. A strategy for the observation of volcanism on Earth from space. *Philos. Trans. R. Soc. Lond. Ser. A Math. Phys. Sci.* **2003**, *361*, 145–156. [[CrossRef](#)] [[PubMed](#)]
68. Aufaristama, M.; Hoskuldsson, A.; Jonsdottir, I.; Ulfarsson, M.; Thordarson, T. New Insights for Detecting and Deriving Thermal Properties of Lava Flow Using Infrared Satellite during 2014–2015 Effusive Eruption at Holuhraun, Iceland. *Remote Sens.* **2018**, *10*, 151. [[CrossRef](#)]
69. Camacho-Alpízar, A.; Fuchs, E.J.; Barrantes, G. Effect of barriers and distance on song, genetic, and morphological divergence in the highland endemic Timberline Wren (*Thryorchilus browni*, Troglodytidae). *PLoS ONE* **2018**, *13*, e0209508. [[CrossRef](#)]
70. Aufaristama, M.; Hoskuldsson, A.; Ulfarsson, M.O.; Jonsdottir, I.; Thordarson, T. The 2014–2015 Lava Flow Field at Holuhraun, Iceland: Using Airborne Hyperspectral Remote Sensing for Discriminating the Lava Surface. *Remote Sens.* **2019**, *11*, 476. [[CrossRef](#)]
71. Li, L.; Solana, C.; Canters, F.; Kervyn, M. Testing random forest classification for identifying lava flows and mapping age groups on a single Landsat 8 image. *J. Volcanol. Geotherm. Res.* **2017**, *345*, 109–124. [[CrossRef](#)]
72. Spinetti, C.; Mazzarini, F.; Casacchia, R.; Colini, L.; Neri, M.; Behncke, B.; Salvatori, R.; Buongiorno, M.F.; Pareschi, M.T. Spectral properties of volcanic materials from hyperspectral field and satellite data compared with LiDAR data at Mt. Etna. *Int. J. Appl. Earth Obs. Geoinf.* **2009**, *11*, 142–155. [[CrossRef](#)]
73. Lary, D.J.; Alavi, A.H.; Gandomi, A.H.; Walker, A.L. Machine learning in geosciences and remote sensing. *Geosci. Front.* **2016**, *7*, 3–10. [[CrossRef](#)]
74. Li, C.; Wang, J.; Wang, L.; Hu, L.; Gong, P. Comparison of classification algorithms and training sample sizes in urban land classification with Landsat thematic mapper imagery. *Remote Sens.* **2014**, *6*, 964–983. [[CrossRef](#)]
75. Lüdtke, A.; Jerosch, K.; Herzog, O.; Schlüter, M. Development of a machine learning technique for automatic analysis of seafloor image data: Case example, Pogonophora coverage at mud volcanoes. *Comput. Geosci.* **2012**, *39*, 120–128. [[CrossRef](#)]
76. Ganci, G.; Cappello, A.; Bilotta, G.; Héroult, A.; Zago, V.; Del Negro, C. 3D Lava flow mapping at Etna volcano from Pléiades-derived DEM differences. *PANGAEA* **2019**. [[CrossRef](#)]
77. Jain, A.K.; Dubes, R.C. *Algorithms for Clustering Data*; Prentice Hall: Englewood Cliffs, NJ, USA, 1988; Volume 6.
78. Christopher, B. *Pattern Recognition and Machine Learning*; Springer: Berlin/Heidelberg, Germany, 2006.
79. Cappello, A.; Ganci, G.; Bilotta, G.; Herault, A.; Zago, V.; Del Negro, C. Satellite-driven modeling approach for monitoring lava flow hazards during the 2017 Etna eruption. *Ann. Geophys.* **2018**, *61*, 13. [[CrossRef](#)]

80. Kereszturi, G.; Cappello, A.; Ganci, G.; Procter, J.; Németh, K.; Del Negro, C.; Cronin, S.J. Numerical simulation of basaltic lava flows in the Auckland Volcanic Field, New Zealand – Implication for volcanic hazard assessment. *Bull. Volcanol.* **2014**, *76*, 879. [[CrossRef](#)]
81. Kereszturi, G.; Nemeth, K.; Vioufti, M.R.; Cappello, A.; Murcia, H.; Ganci, G.; Del Negro, C.; Procter, J.; Zahran, H.M.A. Emplacement conditions of the 1256 AD Al-Madinah lava flow field in Harrat Rahat, Kingdom of Saudi Arabia—Insights from surface morphology and lava flow simulations. *J. Volcanol. Geotherm. Res.* **2016**, *309*, 14–30. [[CrossRef](#)]
82. Cappello, A.; Ganci, G.; Calvari, S.; Perez, N.M.; Hernandez, P.A.; Silva, S.V.; Cabral, J.; Del Negro, C. Lava flow hazard modeling during the 2014–2015 Fogo eruption, Cape Verde. *J. Geophys. Res. Solid Earth* **2016**, *121*, 2290–2303. [[CrossRef](#)]
83. Bilotta, G.; Cappello, A.; Hérault, A.; Vicari, A.; Russo, G.; Del Negro, C. Sensitivity analysis of the MAGFLOW Cellular Automaton model for lava flow simulation. *Environ. Model. Softw.* **2012**, *35*, 122–131. [[CrossRef](#)]
84. Bilotta, G.; Cappello, A.; Hérault, A.; Del Negro, C. Influence of topographic data uncertainties and model resolution on the numerical simulation of lava flows. *Environ. Model. Softw.* **2019**, *112*, 1–15. [[CrossRef](#)]
85. Aufaristama, M.; Höskuldsson, Á.; Jónsdóttir, I.; Ólafsdóttir, R. Mapping and Assessing Surface Morphology of Holocene Lava Field in Krafla (NE Iceland) Using Hyperspectral Remote Sensing. *IOP Conf. Ser. Earth Environ. Sci.* **2016**, *29*, 1–6. [[CrossRef](#)]
86. Bailey, J.E.; Harris, A.J.L.; Dehn, J.; Calvari, S.; Rowland, S.K. The changing morphology of an open lava channel on Mt. Etna. *Bull. Volcanol.* **2006**, *68*, 497–515. [[CrossRef](#)]
87. Kolzenburg, S.; Jaenicke, J.; Münzer, U.; Dingwell, D.B. The effect of inflation on the morphology-derived rheological parameters of lava flows and its implications for interpreting remote sensing data—A case study on the 2014/2015 eruption at Holuhraun, Iceland. *J. Volcanol. Geotherm. Res.* **2018**, *357*, 200–212. [[CrossRef](#)]
88. Pinkerton, H.; James, M.; Jones, A. Surface temperature measurements of active lava flows on Kilauea volcano, Hawai'i. *J. Volcanol. Geotherm. Res.* **2002**, *113*, 159–176. [[CrossRef](#)]



© 2019 by the authors. Licensee MDPI, Basel, Switzerland. This article is an open access article distributed under the terms and conditions of the Creative Commons Attribution (CC BY) license (<http://creativecommons.org/licenses/by/4.0/>).